

# Detectability and Model Discriminability of the Dark Ages 21 cm Global Signal

Shintaro Yoshiura

*Mizusawa VLBI Observatory, National Astronomical Observatory of Japan, 2-21-1 Osawa, Mitaka, Tokyo 181-8588, Japan*<sup>\*</sup>

Fumiya Okamatsu

*Department of Physics, College of Humanities and Sciences, Nihon University, Tokyo, 156-8550, Japan*

Tomo Takahashi

*Department of Physics, Saga University, Saga 840-8502, Japan*

(Dated: February 3, 2026)

The 21 cm signal from neutral hydrogen atom is almost the only way to directly probe the Dark Ages. The Dark Ages 21 cm signal, observed at frequencies below 50 MHz, can serve as a powerful probe of cosmology, as the standard cosmological model predicts a well-defined 21 cm spectral shape. In this work, we assess the detectability and model-selection power of 21 cm observations assuming physically motivated foregrounds, optimistic error levels, and several observing strategies for the signals predicted in various cosmological models. Using a Bayesian evidence-based comparison, we find that wide-band observations covering 1–50 MHz can identify the evidence of non-zero 21 cm signals from models considered in this paper except the one with a smooth spectrum that peaks at lower frequencies. In particular, observations below 15 MHz are essential to avoid degeneracies with the foreground. Furthermore, even with observations measured at 5 MHz intervals over the frequency range 1 – 50 MHz, the 21 cm signal can be identified if the errors are sufficiently small. This indicates that the intrinsic 21 cm spectral shape can be captured without foreground degeneracy even with a limited number of frequency channels.

## I. INTRODUCTION

During the Dark Ages, before the formation of the first stars, the Universe was filled with neutral hydrogen gas. The highly redshifted 21 cm line from this gas, observed at radio frequencies, observed at radio frequencies, gives the only direct probe of the Dark Ages [1, 2]. The Dark Ages 21 cm signal can provide a stringent test of cosmological models as it can be predicted solely from cosmology, free from astrophysical uncertainties. In the standard  $\Lambda$ CDM cosmology, the signal appears as an absorption feature with a depth of  $-40$  mK at the peak frequency 15 MHz. In [3], the consistency ratio—defined as the ratio of the signals at a few frequency points—does not change in  $\Lambda$ CDM even when the cosmological parameters are varied, and can effectively distinguish alternative cosmological models.

After the Dark Ages, the Cosmic Dawn and Epoch of Reionization eras follow, where the 21 cm line can be a powerful observable to understand astrophysics such as when and what types of stars formed and how the Universe was heated. To date, several ground-based instruments have been used to probe the sky-averaged 21 cm signal; EDGES reported a strong absorption feature at a redshift of 17.8 [4]. While systematic effects have been claimed [5–9] and a follow-up observation with SARAS3 did not detect the signal [10], which motivated many theoretical studies to construct models explaining the EDGES result or to constrain existing models (see, e.g.,

[11] and the references therein). Interestingly, some proposed models predict an enhanced signal during the Dark Ages. Thus, the 21 cm line from this era remains a powerful probe of such models, even in light of later cosmic epochs, and follow-up observations below 50 MHz are highly anticipated.

In light of this background, several projects aim to detect the sky-averaged 21 cm signal from the Dark Ages, using moon orbiting satellite (e.g. CosmoCube [12], DAPPER[13], DARE[14], DSL [15], NCLE [16], PRATUSH [17], SEAMS[18], TREED [19, 20]) and using moon lander (e.g. DEX [21], FAR SIDE [22], LARAF [23], LuSEE-Night [24], TSUKUYOMI [25, 26]). These projects are designed to measure the signal from outside the Earth to avoid ionospheric effects. In addition, radio-frequency interference (RFI) is also a major obstacle, which could be mitigated by observing the signal from the lunar far side.

Even if RFI can be reduced in this way, the most significant challenge arises from astrophysical foregrounds, dominated by synchrotron emission from our Galaxy, with contributions from free-free emission and emission from extragalactic radio sources, which can reach the noise level of  $10^5$  K at 15 MHz. Thus, careful treatment of systematic errors is essential. For example, accurate instrument calibration and proper modeling of reflected-wave noise parameters are required to avoid non-smooth spectral structures [27]. In addition, the chromaticity of the instrumental beam can create unwanted spectral structure due to the anisotropy of the foreground emission. A possible approach to avoid this issue is to measure a few frequencies with a variable-length dipole to achieve a stable instrumental beam shape over a wide frequency

---

<sup>\*</sup> shintaro.yoshiura@nao.ac.jp

range, whereas a dipole measuring a wide band can suffer from large loss and beam chromaticity, which is motivated by the results of [3] and is planned to be adopted in the TREED project. A similar concept for ground-based observations has also been proposed in [28].

The first milestone for the Dark Ages 21 cm line is the detection of a non-zero signal, regardless of accuracy or model discrimination. In this work, therefore, we verify the detectability of the signal and also investigate the ability of model selection by taking several 21 cm signal models as examples with a physically motivated foreground modeling and assuming observing strategies motivated by recent projects. Throughout this work, we employ Bayesian evidence, which has been used in many previous works related to global 21 cm signal analyses e.g. [29–35], as a metric for detection and model selection.

This paper is organized as follows. In Section II, we introduce our statistical metric and several cosmological models for the 21 cm signal, and discuss foregrounds, instrumental noise, and observing strategies. In Section III, we present our results and examine the detectability and model-selection power of selected observing strategies. Section IV summarizes this work.

## II. METHOD

As a statistical metric, we employ the Bayesian evidence. Here we briefly describe it by following [32]. For a data set  $D$ , a model  $M_i$ , and model parameters  $\Theta$ , the posterior distribution of the parameters is given by

$$P(\Theta|D, M_i) = \frac{P(D|\Theta, M_i)P(\Theta|M_i)}{P(D|M_i)}, \quad (1)$$

where  $P(\Theta|M_i)$  is the prior distribution,  $P(D|\Theta, M_i)$  is the likelihood, and  $P(D|M_i) \equiv Z_i$  is the Bayesian evidence. To evaluate  $Z_i$ , we use POLYCHORD [36, 37], which performs nested sampling. For the purpose of model comparison, the Bayes factor defined by the ratio of the Bayesian evidences of two models  $\Delta \ln Z_{i,j} = \ln Z_i - \ln Z_j$ , can be used. The Bayes factor quantifies the odds of model  $i$  relative to model  $j$  when equal prior probabilities are assigned to the models. This quantity is commonly interpreted as follows [38]: (1)  $\Delta \ln Z_{i,j} < 1$ , for which the evidence is “not worth more than a bare mention”; (2)  $1 < \Delta \ln Z_{i,j} < 3$ , positive; (3)  $3 < \Delta \ln Z_{i,j} < 5$ , strong; and (4)  $5 < \Delta \ln Z_{i,j}$ , very strong.

The 21 cm signal is proportional to  $1 - T_\gamma/T_S$ , where  $T_\gamma$  is the radio background temperature and  $T_S$  is the spin temperature. The spectral shape of the 21 cm signal depends on the physical processes that affect the spin temperature and the kinetic gas temperature. The details of the 21 signal are given, e.g., in [1, 2].

In this work, we employ eight models for the 21 cm signal in [3, 39] where the 21 cm signal are calculated by modifying RECFAST [40–43]. Figure 1 shows

these signals. In addition to the eight models labeled by  $i$  ( $i = 1\text{--}8$ ), we also consider a model with no 21 cm signal ( $i = 0$ , NO21). For all models, the cosmological parameters are assumed as  $\Omega_b h^2 = 0.02237$ ,  $\Omega_m h^2 = 0.14237$ ,  $Y_p = 0.2436$  and  $H_0 = 67.36 \text{ km s}^{-1} \text{ Mpc}^{-1}$ .

Here we briefly describe the characteristics of the 21 cm models which will be considered in this paper. Details are given in [3, 39].

- **(1:  $\Lambda$ CDM)** This model corresponds to the standard 21 cm signal in  $\Lambda$ CDM. The absorption trough is centered at 15 MHz with an amplitude of 40 mK.
- **(2: DMBw)** This is the weak DM–baryon (DMB) coupling model [44]. Gas cooling driven by dark matter–baryon coupling leads to a stronger absorption signal.
- **(3: DMBs)** The underlying model is the same as DMBw, but with stronger cooling by assuming a larger scattering cross section between DM and baryon.
- **(4: EDE)** Early dark energy (EDE) leads to earlier decoupling between photons and baryons due to the change of the expansion rate [45]. As a result, the gas temperature can be lower than in  $\Lambda$ CDM, and the absorption amplitude becomes deeper.
- **(5: ERB)** This model assumes an excess radio background (ERB) in addition to the CMB [46]. Because the 21 cm signal is defined as an absorption signal against the radio background, a stronger absorption signal is expected with an excess radio background.
- **(6: LDMD)** Light dark matter decay (LDMD) heats the gas even without stars, which makes the absorption trough shallower [47].
- **(7: PMFw)** Primordial magnetic field (PMF) can weakly heat the gas via decaying magnetic turbulence and ambipolar diffusion, which results in shallower absorption trough.
- **(8: PMFs)** The underlying model is the same as PMFw, however, when the heating is too effective, the 21 cm signal appears as emission line.

The radio background temperature is given by  $T_R = T_{\text{cmb}} + T_{\text{ER}} (\nu/\nu_{78})^{-2.6}$  with  $T_{\text{ER}} = 0.03 \text{ K}$  for the ERB model, and by  $T_R = T_{\text{cmb}}$  for the other models.

This work does not aim to interpret the physical origin of the 21 cm models, but instead examines the signal shape to investigate which types of 21 cm signals can be detected or differentiated. Table I summarizes the peak amplitude and the peak frequency, except for ERB, because the ERB model does not exhibit an absorption trough. Most models have their peak at around 15 MHz. Compared with  $\Lambda$ CDM, models such as DMBw, DMBs

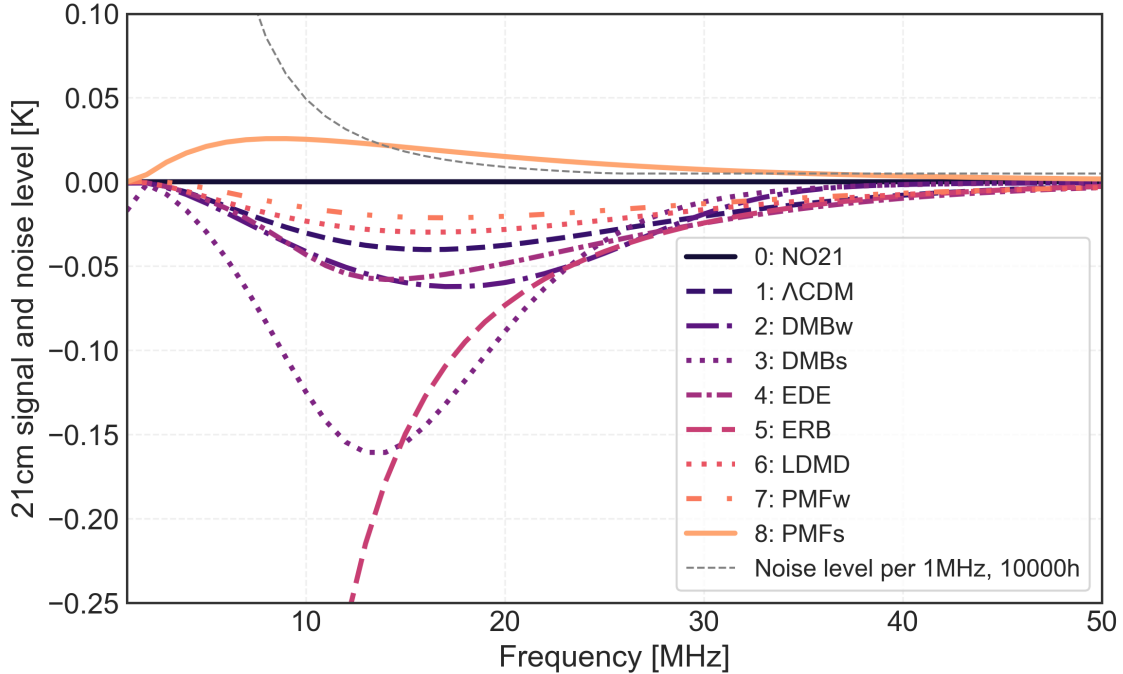


FIG. 1. The 21 cm signal spectra used in this work for model comparison. There are nine models: eight cosmological models ( $i = 1-8$ ) and one zero-signal model ( $i = 0$ ). The thin dashed line shows the thermal-noise level assuming 10,000 hours of integration time.

TABLE I. Summary of spectral features (the absorption peak and the peak frequency) of the 21 cm models employed in this work.

Model	peak [mK]	peak $\nu$ [MHz]
1: $\Lambda$ CDM	-40.1	16
2: DMBw	-62.1	17
3: DMBs	-160.6	14
4: EDE	-57.9	14
5: ERBs	-	-
6: LDMD	-29.8	16
7: PMFw	-21.3	17
8: PMFs	25.7	9

and EDE exhibit strong absorption, whereas LDMD and PMFw show weak absorption. An exception is the PMFs model which produces an emission feature at around 15 MHz.

For the likelihood analysis, we fix the model and cosmological parameters for each 21 cm model and evaluate the detection and model-selection performance, which is the primary objective of this work. Fixing the cosmological parameters does not affect our conclusions, since the shapes of the 21 cm signals in  $\Lambda$ CDM and in models beyond  $\Lambda$ CDM vary only weakly within the parameter ranges allowed by current observations [3].

In principle, the nested-sampling algorithm can be used to infer posterior distributions of the model parameters for each extended 21 cm scenario. However, accurate

predictions for some models are computationally expensive, making a full nested-sampling analysis impractical. Therefore, in this work, we instead test the feasibility of model selection for a representative set of 21 cm signal models.

In addition to the 21 cm signal, the foreground should also be included as it dominates the signal. Although polynomial functions are also commonly used to model the foreground spectrum, they may carry some risk of producing non-physical spectra. In practice, model selection can be performed with multiple foreground models [29, 32]. In this work, we adopt a physically motivated foreground model based on [48]:

$$T_{\text{FG}} = T_G (\nu/\nu_{10})^{\alpha-2} \left( \frac{1 - \exp(-\tau_\nu)}{\tau_\nu} \right) + T_{\text{eg}} (\nu/\nu_{10})^{\beta-2} \exp(-\tau_\nu), \quad (2)$$

$$\nu_{10} = 10 \text{ MHz} \text{ and } \tau_\nu = F \nu^{-2.1}.$$

The first term corresponds to synchrotron emission from the Galaxy, while the second term describes the extragalactic foreground component subject to free-free absorption. We adopt an optical depth of  $\tau_\nu = F \nu^{-2.1}$ . The optically thick region also attenuates the 21 cm signal and the radio background [49].

As the mock foreground temperature, which is used as true foreground model  $f_t$ , the following parameter values are assumed [48]:  $T_G, T_{\text{eg}}, \alpha, F, \beta = 2.45 \times 10^5 \text{ K}, 5.5 \times 10^4 \text{ K}, 0.515, 5, 0.8$ . This true model is fitted with the following parameter ranges:  $1.95 \times 10^5 < T_G < 2.95 \times 10^5$ ,

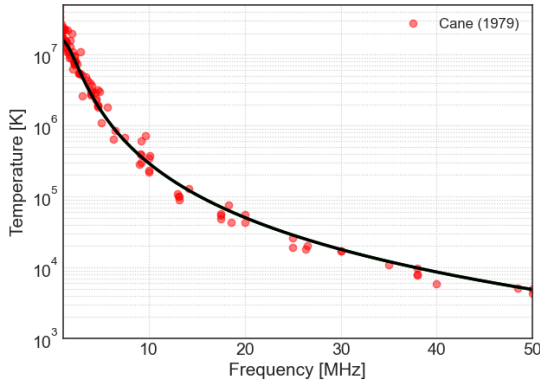


FIG. 2. The solid line shows the foreground model used to generate the mock data. The red dots show the observed values from [48].

$5.0 \times 10^4 < T_{\text{eg}} < 6.0 \times 10^4$ ,  $0.4 < \alpha < 0.6$ ,  $4 < F < 6$ , and  $0.5 < \beta < 1.0$ . Figure 2 shows the mock foreground model and the observed values listed in [48]. It should be noted that the foreground temperature reaches  $10^7$  K at 1 MHz.

Designing instruments optimized for observing the Dark Ages is challenging because of the large frequency dynamic range. Thus, non-optimized instruments may have low radiation efficiency. To reduce systematics, it can be useful to introduce an attenuator between an antenna and a receiver [27, 50] while the attenuator adds noise. Here, we allow the receiver noise temperature, including attenuator noise, to be as high as 3000 K, which is the same level as the foreground power at 50 MHz.

Combining the foreground and instrumental noise, the thermal-noise level is then given by  $\sigma = (T_{\text{sky}} + T_{\text{rec}})/\sqrt{\Delta t \Delta \nu}$ , where the sky temperature is  $T_{\text{sky}} = f_t$ , the receiver noise is  $T_{\text{rec}}$ ,  $\Delta t$  is the integration time per channel, and the channel width is  $\Delta \nu = 1$  MHz.

It is not easy to predict and model instrumental systematic errors, such as calibration errors [27], ionospheric effects [51], and beam chromaticity [52]. In this work, to investigate the ideal detectability, we do not include complicated systematic errors. On the other hand, we assume a minimum noise level of 5 mK in each channel as a fiducial value. This choice is motivated by requiring that the wide-band observation can detect the  $\Lambda$ CDM model, as described in Section III.

For the observing configurations, we assume the following three cases: (1) observations from 1 MHz to 50 MHz with a wide-band antenna and a channel width of 1 MHz; (2) observations from 1 MHz to 50 MHz at 5 MHz intervals, using an optimized antenna for each frequency channel with a bandwidth of 1 MHz; and (3) observations from 15 MHz to 50 MHz with a wide-band antenna and a channel width of 1 MHz. For configurations (1) and (3), a wide-band antenna may introduce unwanted spectral structure due to instrumental chromaticity. For configu-

ration (2), we assume independent instruments optimized for each channel, which may reduce systematic errors. These strategies are motivated by the findings of [3].

Using models of the 21 cm signal, foregrounds, and noise, together with the assumed observing configurations, we assess the detection and model-selection performance via Bayesian evidence. For this purpose, we construct mock data based on the 21 cm signal of model  $i$ , as described in the the previous section. The mock signal at the  $k$ -th frequency channel, including foreground, is given by

$$D_{i,k} = (m_i + T_{R,t}) \exp(-\tau_\nu) + f_t, \quad (3)$$

where  $m_i$  is the true 21 cm signal for model  $i$ , and  $f_t$  and  $T_{R,t}$  denote the mock foreground and radio background temperature, respectively. We then fit the model  $j$  to the mock data constructed from model  $i$ . The model prediction at the  $k$ -th frequency channel is given by

$$M_{j,k} = (m_j + T_{R,j}) \exp(-\tau_\nu) + f_s(\Theta), \quad (4)$$

where  $m_j$  denotes the 21 cm signal, and  $f_s(\Theta)$  and  $T_{R,j}$  represent the foreground and radio background temperature, respectively, of the model fitted to the mock data. We note that, except for the EBR model,  $T_{R,t}$  and  $T_{R,s}$  are set equal to  $T_{\text{cmb}}$ . Then we define a Gaussian likelihood as

$$\ln L_j(\Theta) = -\frac{1}{2} \sum_k \left[ \ln(2\pi\sigma_k^2) + \frac{(D_k - M_k(\Theta))^2}{\sigma_k^2} \right], \quad (5)$$

with  $\sigma_k$  is the noise level at the  $k$ -th frequency channel. With this likelihood, we assess the detectability and model discriminability in the next section.

### III. RESULTS & DISCUSSION

#### A. Detectability

In this section, we discuss the detectability for several observing strategies described in the previous section. Specifically, using mock data generated from the true 21 cm model  $i$ , we compare the evidence  $\ln Z_i$ , obtained with fitted model  $j = i$ , with  $\ln Z_0$  for the NO21 model ( $j = 0$ ). If  $\Delta \ln Z_{i,0} = \ln Z_i - \ln Z_0$  is greater than 1, we interpret the observation as detectable, since the data favor a model  $i$  suggests that a model with a non-zero signal is more supported by the data than the model without a 21 cm signal.

This “detectability” should be interpreted as evidence-based preference rather than a frequentist detection significance.

Table II lists the results for observations covering 1 MHz to 50 MHz continuously with a wide-band antenna. The results show that this observing configuration has strong detectability for most 21 cm models, except for the PMFs model.

TABLE II. Detectability for observations covering 1 MHz to 50 MHz with an integration time of 10,000 hours. Evidence interpretation is based on [38].

Model	$\ln Z_1$ ( $i = j$ )	$\ln Z_2$ ( $j = 0$ )	$\Delta \ln Z_{1,2}$	Evidence
True M	True M	(NO21)		
1: $\Lambda$ CDM	101.08	92.18	8.90	very strong
2: DMBw	101.00	45.55	55.44	very strong
3: DMBs	101.19	30.76	70.43	very strong
4: EDE	101.29	89.24	12.05	very strong
5: ERB	100.62	98.25	2.37	positive
6: LDMD	100.85	97.53	3.32	strong
7: PMFw	100.83	99.61	1.21	positive
8: PMFs	100.85	101.14	-0.29	not worth

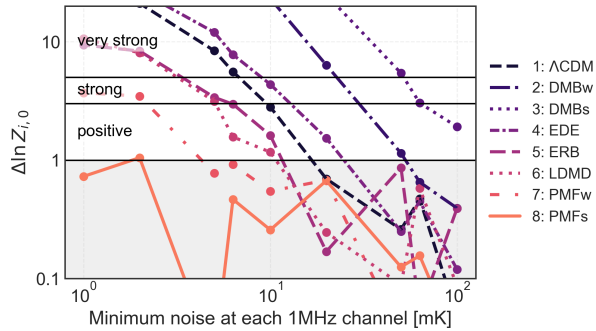


FIG. 3. Dependence of  $\Delta \ln Z_{i,0}$  on the assumed minimum noise level in each 1 MHz channel. The three horizontal lines indicate the interpretation thresholds for  $\Delta \ln Z_{i,0}$ .

To interpret the results more carefully, Figure 4 shows the residual signal obtained by subtracting the foreground, evaluated at the maximum-likelihood parameters, using the NO21 as subtracted model data ( $j = 0$ ). For most models, the residual signal after foreground subtraction exhibits a significant deviation from zero in the 15–50 MHz range. In the PMFs model, however, the residual remains below the noise level at all frequencies, indicating a weak signal whose shape is partially absorbed by the foreground model.

We next assess the minimum noise level required to detect the 21 cm signal. Figure 3 shows  $\Delta \ln Z_{i,0}$  as a function of the minimum noise levels, for a wide-band observation from 1 MHz to 50 MHz. With a noise level of 100 mK, none of the models are detected with strong evidence ( $\Delta \ln Z_{i,0} > 3$ ). The PMFs model remains undetectable even at a 1 mK noise floor. The  $\Lambda$ CDM model can be detected with very strong evidence ( $\Delta \ln Z_{i,0} > 5$ ) at 5 mK. Therefore, we adopt 5 mK as the fiducial noise level.

We next assume observations at 5 MHz intervals spanning from 1 MHz to 50 MHz. This observing strategy is motivated by [3], which demonstrates that a few frequency points are sufficient to distinguish between cosmological models. This observing strategy corresponds either to measurements at a small number of targeted

TABLE III. Same as Table II, but assuming measurements at 1, 5, 10, 15, 20, 25, 30, 35, 40, 45, and 50 MHz.

Model	$\ln Z_1$ ( $i = j$ )	$\ln Z_2$ ( $j = 0$ )	$\Delta \ln Z_{1,2}$	Evidence
True M	True M	(NO21)		
1: $\Lambda$ CDM	-24.50	-25.32	0.82	not worth
2: DMBw	-24.79	-27.81	3.02	strong
3: DMBs	-24.25	-27.26	3.01	strong
4: EDE	-24.64	-25.19	0.55	not worth
5: ERB	-24.45	-25.14	0.68	not worth
6: LDMD	-24.21	-24.80	0.59	not worth
7: PMFw	-24.41	-24.39	-0.02	not worth
8: PMFs	-24.80	-24.28	-0.52	not worth

TABLE IV. Same as Table III, but assuming minimum noise level is 1 mK and reduction of noise level by a factor of  $1/\sqrt{5}$ .

Model	$\ln Z_1$ ( $i = j$ )	$\ln Z_2$ ( $j = 0$ )	$\Delta \ln Z_{1,2}$	Evidence
True M	True M	(NO21)		
1: $\Lambda$ CDM	-16.87	-24.44	7.57	very strong
2: DMBw	-16.99	-43.27	26.29	very strong
3: DMBs	-16.89	-47.36	30.47	very strong
4: EDE	-17.39	-24.31	6.93	very strong
5: ERB	-16.96	-18.95	1.99	positive
6: LDMD	-16.97	-20.18	3.21	strong
7: PMFw	-16.81	-18.65	1.84	positive
8: PMFs	-17.42	-16.92	-0.49	not worth

frequencies using independently optimized instruments, or to wide-band observations in which many channels are lost due to RFI. The results for this strategy are given in Table III, showing that the detectability is lower than that in Table II. Nevertheless, the DMBw and DMBs models can be detected with this observing configuration, indicating that observations at a few frequency channels are in principle sufficient to detect the 21 cm signal. However, this configuration fails to detect the  $\Lambda$ CDM model.

From the above arguments, it remains unclear whether the limiting factor in detecting the 21 cm signal is the sensitivity or the number of frequency channels. A closer examination of  $\Lambda$ CDM, EDE, ERB, and LDMD in Table III where  $\Delta \ln Z_{i,0} > 0.5$ , suggesting that improving the sensitivity enhances detectability. For illustration, we assume a minimum noise level of 1 mK for measurements at 5 MHz intervals, for comparison with the wide-band observation. The noise level is reduced by a factor of  $1/\sqrt{5}$ , reflecting the number of channels: 50 for the wide-band and 11 for the limited-channel setup. The resulting detectability, shown in Table IV, is consistent with the wide-band results in Table II. These findings indicate that the degradation in detectability is primarily due to sensitivity. In other words, with sufficient sensitivity, even observations at a few selected channels can reliably measure the 21 cm signal in the presence of foregrounds.

For detecting the Dark Ages 21 cm signal, it is a

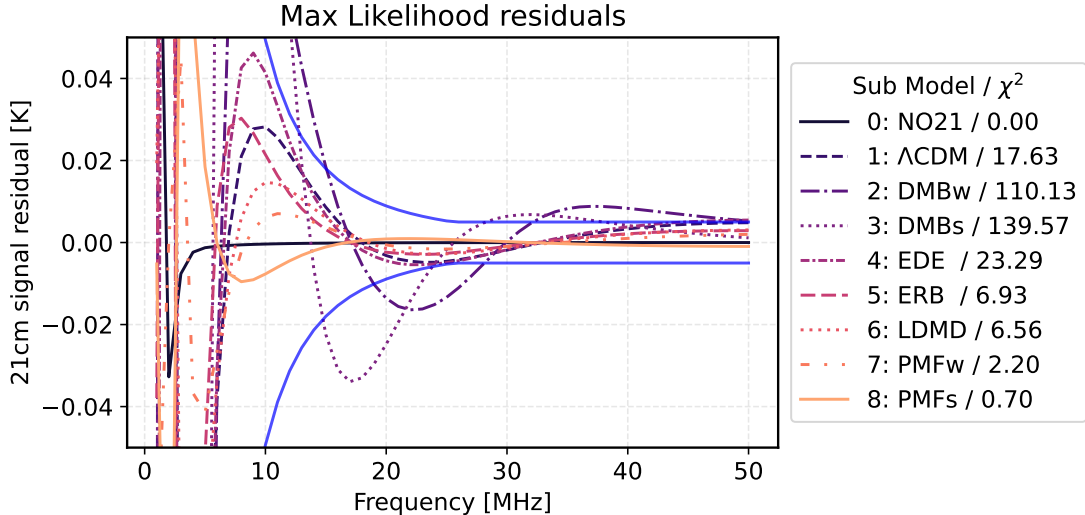


FIG. 4. Residuals after foreground subtraction using the maximum-likelihood parameter sample for the case  $j = 0$ . The two blue lines indicate the noise level for reference.

TABLE V. Same as Table II, but assuming the measurement at 15–50 MHz.

Model	$\ln Z_1$ ( $i = j$ )	$\ln Z_2$ ( $j = 0$ )	$\Delta \ln Z_{i,j}$	Evidence
True M (NO21)				
1: $\Lambda$ CDM	106.61	106.36	0.25	not worth
2: DMBw	106.08	105.16	0.91	not worth
3: DMBs	106.68	105.81	0.87	not worth
4: EDE	105.86	107.13	-1.27	not worth
5: ERB	106.48	106.39	0.10	not worth
6: LDMD	106.33	106.18	0.16	not worth
7: PMFw	106.54	106.46	0.08	not worth
8: PMFs	106.36	106.50	-0.14	not worth

common strategy to observe from outside the Earth to avoid ionospheric reflection. Nonetheless, even though ionospheric refraction and RFI cannot be fully avoided, ground-based observations can probe frequencies down to 10–20 MHz. Thus, we also assess the detectability of a wide-band observation covering 15–50 MHz. Table V shows the results. Notably, this observing configuration fails to detect any of the 21 cm models. This suggests that observations below 15 MHz are essential to distinguish the 21 cm signal from the foreground under our assumptions, motivating space-based measurements at these frequencies to probe the Dark Ages signal. It is worth noting that  $\Delta \ln Z_{i,0}$  for DMBw and DMBs exceeds 0.8, suggesting that increased sensitivity could enable their detection.

## B. Model Discriminability

In the previous subsection, we focused on  $\ln Z$  for the mock  $i = 1$ –8, using the fitted data constructed from no 21 cm signal model ( $j = 0$ ; NO21), and discussed the detectability. In this section, we present results on the model discriminability by generating mock data from each model  $i$  and fitting a different model  $j$  ( $\neq i$ ).

Figure 5 summarizes  $\Delta \ln Z_{i,j} = \ln Z_i - \ln Z_j$  for all combinations of true model  $i$  and fitted model  $j$  for a wide-band observation covering 1 MHz–50 MHz. The mock data contain the 21 cm signal corresponding to model  $i$ . We compare the evidence  $\ln Z_i$  obtained when model  $i$  is assumed in the fit with the evidence  $\ln Z_j$  obtained when model  $j$  is assumed in the fit. If  $\Delta \ln Z_{i,j} > 1$ , model  $i$  is favored over model  $j$ . The color of each cell indicates the magnitude of  $\Delta \ln Z_{i,j}$ .

To aid interpretation of the results, we plot the residuals after model subtraction using the maximum-likelihood parameters in Figure 6. In addition, we also calculate the value of  $\chi^2$ , given as

$$\chi^2 = \sum_k \frac{(D_{i,k} - M_{j,k}(\Theta))^2}{\sigma_k^2}, \quad (6)$$

which is also shown in the legend of the figure. In most cases with  $\Delta \ln Z_{i,j} > 1$ , the  $\chi^2$  is larger than 2 and the residuals exhibit peaks within 20–50 MHz. This suggests that  $\Delta \ln Z_{i,j} > 1$  provides a reliable criterion for model discriminability.

Now let us look at each true model in Figure 6. For the NO21 case ( $i = 0$ ), the true model is strongly favored over all models except PMFs. This suggests that foreground partially absorbs the signal, since the PMFs model has a weak and smooth structure above 10 MHz. As shown in

the top-left panel of Figure 6, the residuals are consistent with zero at  $\nu > 20$  MHz.

For the  $\Lambda$ CDM case ( $i = 1$ ),  $\Lambda$ CDM is distinguishable from all models except EDE. This reflects the similarity of the 21 cm signals in  $\Lambda$ CDM and EDE, and the residuals are consistent with zero (top-right panel of Figure 6).

For the DMBw ( $i = 2$ ) and DMBs ( $i = 3$ ) cases, very strong model-selection power is found against all other models. The residuals exhibit negative peaks around 21 MHz and 18 MHz, and positive peaks around 35 MHz and 29 MHz for DMBw and DMBs, respectively (second row of Figure 6).

For the EDE case ( $i = 4$ ), because the 21 cm signal is similar to  $\Lambda$ CDM, the results are similar to those for the  $\Lambda$ CDM ( $i = 1$ ) case.

The ERB, LDMD, and PMFw models ( $i = 5, 6, 7$ ) cannot be distinguished from one another. LDMD and PMFw are similar to each other, but both differ from ERB. This suggests that most of the ERB 21 cm signal is degenerate with the foreground model, and the residual after subtraction remains below the noise level.

For the PMFs case ( $i = 8$ ), because the true 21 cm signal is positive and peaks at lower frequencies, the observation has sufficient model-selection power. However, because the signal can be absorbed by the foreground, the residuals are consistent with zero for the  $j = 0$  (NO21) case.

We next consider observations at 5 MHz intervals from 1 MHz to 50 MHz. Figure 7 shows the results. Compared to the wide-band observation, the model-selection power is somewhat reduced. In particular, models with weak signals (EDE, LDMD, PMFw) and smooth spectra (ERB) cannot be distinguished under this observing configuration. However, even with the limited channels, the DMBw and DMBs models remain distinguishable from the other models, and the  $\Lambda$ CDM and PMFs models can also be distinguished from each other.

As in the previous subsection, we also analyze an idealized case assuming a minimum noise level of 1 mK and a reduction by a factor of  $\sqrt{5}$  for observations performed at 5 MHz intervals from 1 MHz to 50 MHz. Figure 8 shows the results, which indicate that the model-selection power is broadly consistent with that shown in Figure 7. We again emphasize that the spectral structure of the 21 cm signal can be captured with a limited number of frequency channels and distinguished from the foreground. As discussed in the previous section, when the frequency range is restricted to 15–50 MHz, the model-selection power is significantly weakened, except for the DMBw model. For robust model selection, regardless of the number of channels, observations covering a sufficiently wide frequency range are required.

To further improve model-selection power, additional information on the foreground would be highly beneficial. For example, SKA1-Low covers frequencies down to 50 MHz and offers significantly better sensitivity than existing instruments. Such observations could constrain the parameters of the extragalactic foreground temperature

at 50 MHz. Since Galactic diffuse emission exhibits an anisotropic distribution, whereas the 21 cm signal is expected to be spatially uniform, the direction-dependent component of the foreground may help foreground removal [53, 54]. In practice, free-free absorption by H II regions introduces anisotropic structures in the global 21 cm spectrum [49]. Therefore, accurate foreground removal requires proper modeling of the sky and error characterization [55, 56]. We leave these studies for future work.

In this study, we do not include realistic systematic errors, which may be spectrally non-smooth, because the primary purpose of this work is to assess the detection and model-selection power under ideal conditions. In practice, there are several instrumental (e.g., beam effects and calibration) and observational (e.g., ionospheric effects and RFI) systematics. Although we assume a fiducial minimum noise level of 5 mK, the covariance of systematic errors between different channels may be non-zero. In such cases, wide-band observations can be limited by these systematics, and sophisticated mitigation techniques will be required.

#### IV. SUMMARY

We assessed the detectability of the 21 cm signal under several observing strategies. By employing nine 21 cm models and a physically motivated foreground model, we performed a Bayesian analysis using a nested-sampling algorithm. The likelihood was evaluated by varying the foreground parameters while fixing the 21 cm signal model assumed in the fit, which is subtracted from the mock observed data. Based on the Bayes factor analysis, we found that a wide-band observation covering 1–50 MHz provides strong detection and model-selection power for most 21 cm models. In contrast, a wide-band observation restricted to 15–50 MHz fails to detect the 21 cm signal. Although observations with a limited number of channels suffer from reduced detectability due to insufficient sensitivity, such observations can achieve detection for most models if higher sensitivity is assumed. This implies that a small number of channels can be sufficient to distinguish the 21 cm signal from the foreground owing to intrinsic differences in spectral shape. On the other hand, even wide-band observations cannot detect models with a smooth 21 cm signal that peak below 10 MHz when the frequencies below 15 MHz are excluded.

#### ACKNOWLEDGMENTS

We thank to members of TREED project for their support. We also thank to Teppei Minoda for their fruitful discussion on the modelling of the primordial magnetic fields.

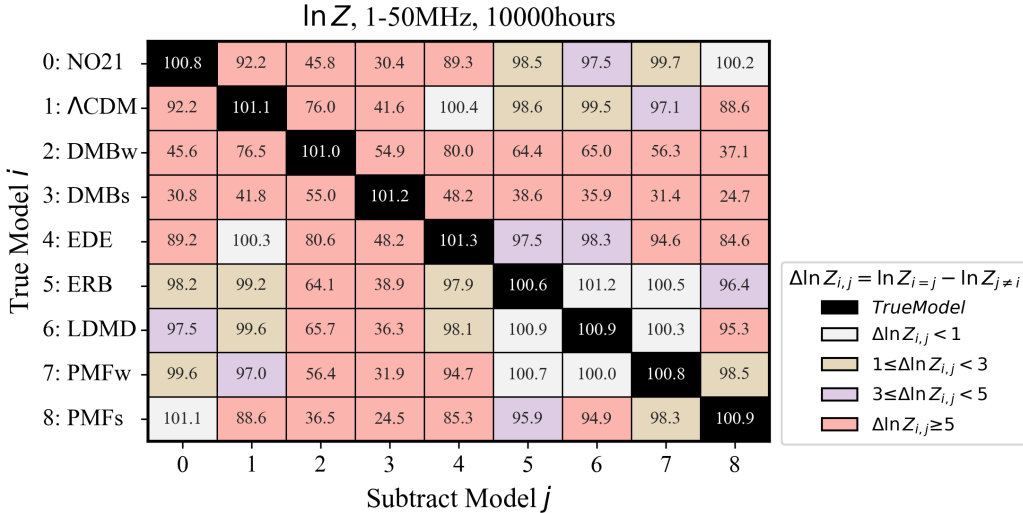


FIG. 5.  $\ln Z$  values for multiple combinations of input and subtraction models assuming a wide-band observation from 1 MHz to 50 MHz. Here,  $i$  is the input model and  $j$  is the subtraction model.

This research was supported by the grant of OML Project by the National Institutes of Natural Sciences (NINS program No, OML022303, OML022402, OML022502). This work is partially supported by JSPS KAKENHI (Grant Number 24K17098(SY),

24K00625(SY), 25K01004 (TT)) and MEXT KAKENHI (Grant Number 23H04515 (TT), 25H01543 (TT)). F.O. is supported by individual research funding from Nihon University.

We acknowledge the use of an AI-based writing tool for language editing.

- 
- [1] S. R. Furlanetto, S. P. Oh, and F. H. Briggs, Cosmology at low frequencies: The 21 cm transition and the high-redshift Universe, *Phys. Rep.* **433**, 181 (2006), arXiv:astro-ph/0608032 [astro-ph].
- [2] J. R. Pritchard and A. Loeb, 21 cm cosmology in the 21st century, *Reports on Progress in Physics* **75**, 086901 (2012), arXiv:1109.6012 [astro-ph.CO].
- [3] F. Okamatsu, T. Minoda, T. Takahashi, D. Yamauchi, and S. Yoshiura, Dark Age Consistency in the 21 cm Global Signal, *Phys. Rev. Lett.* **133**, 131001 (2024), arXiv:2309.06762 [astro-ph.CO].
- [4] J. D. Bowman, A. E. E. Rogers, R. A. Monsalve, T. J. Mozdzen, and N. Mahesh, An absorption profile centred at 78 megahertz in the sky-averaged spectrum, *Nature* **555**, 67 (2018), arXiv:1810.05912 [astro-ph.CO].
- [5] R. Hills, G. Kulkarni, P. D. Meerburg, and E. Puchwein, Concerns about modelling of the EDGES data, *Nature* **564**, E32 (2018), arXiv:1805.01421 [astro-ph.CO].
- [6] R. F. Bradley, K. Tauscher, D. Rapetti, and J. O. Burns, A Ground Plane Artifact that Induces an Absorption Profile in Averaged Spectra from Global 21 cm Measurements, with Possible Application to EDGES, *ApJ* **874**, 153 (2019), arXiv:1810.09015 [astro-ph.IM].
- [7] S. Singh and R. Subrahmanyan, The Redshifted 21 cm Signal in the EDGES Low-band Spectrum, *ApJ* **880**, 26 (2019), arXiv:1903.04540 [astro-ph.CO].
- [8] H. T. J. Bevins, W. J. Handley, A. Fialkov, E. de Lera Acedo, L. J. Greenhill, and D. C. Price, MAXSMOOTH: rapid maximally smooth function fitting with applications in Global 21-cm cosmology, *MNRAS* **502**, 4405 (2021), arXiv:2007.14970 [astro-ph.CO].
- [9] J. Cang, A. Mesinger, S. G. Murray, D. Breitman, Y. Qin, and R. Trotta, The EDGES measurement disfavors an excess radio background during the cosmic dawn, *A&A* **698**, A152 (2025), arXiv:2411.08134 [astro-ph.CO].
- [10] S. Singh, N. T. Jishnu, R. Subrahmanyan, N. Udaya Shankar, B. S. Girish, A. Raghunathan, R. Somashankar, K. S. Srivani, and M. Sathyana Rayana Rao, On the detection of a cosmic dawn signal in the radio background, *Nature Astronomy* **6**, 607 (2022), arXiv:2112.06778 [astro-ph.CO].
- [11] T. Minoda, S. Saga, T. Takahashi, H. Tashiro, D. Yamauchi, S. Yokoyama, and S. Yoshiura, Probing the primordial Universe with 21 cm line from cosmic dawn/epoch of reionization, *PASJ* **75**, S154 (2023), arXiv:2303.07604 [astro-ph.CO].
- [12] K. Artuc and E. de Lera Acedo, The spectrometer development of CosmoCube, lunar orbiting satellite to detect 21-cm hydrogen signal from cosmic dark ages, *RAS Techniques and Instruments* **4**, rzae061 (2025), arXiv:2406.10096 [astro-ph.IM].
- [13] J. Burns, S. Bale, N. Bassett, J. Bowman, R. Bradley, A. Fialkov, S. Furlanetto, M. Hecht, M. Klein-Wolt,

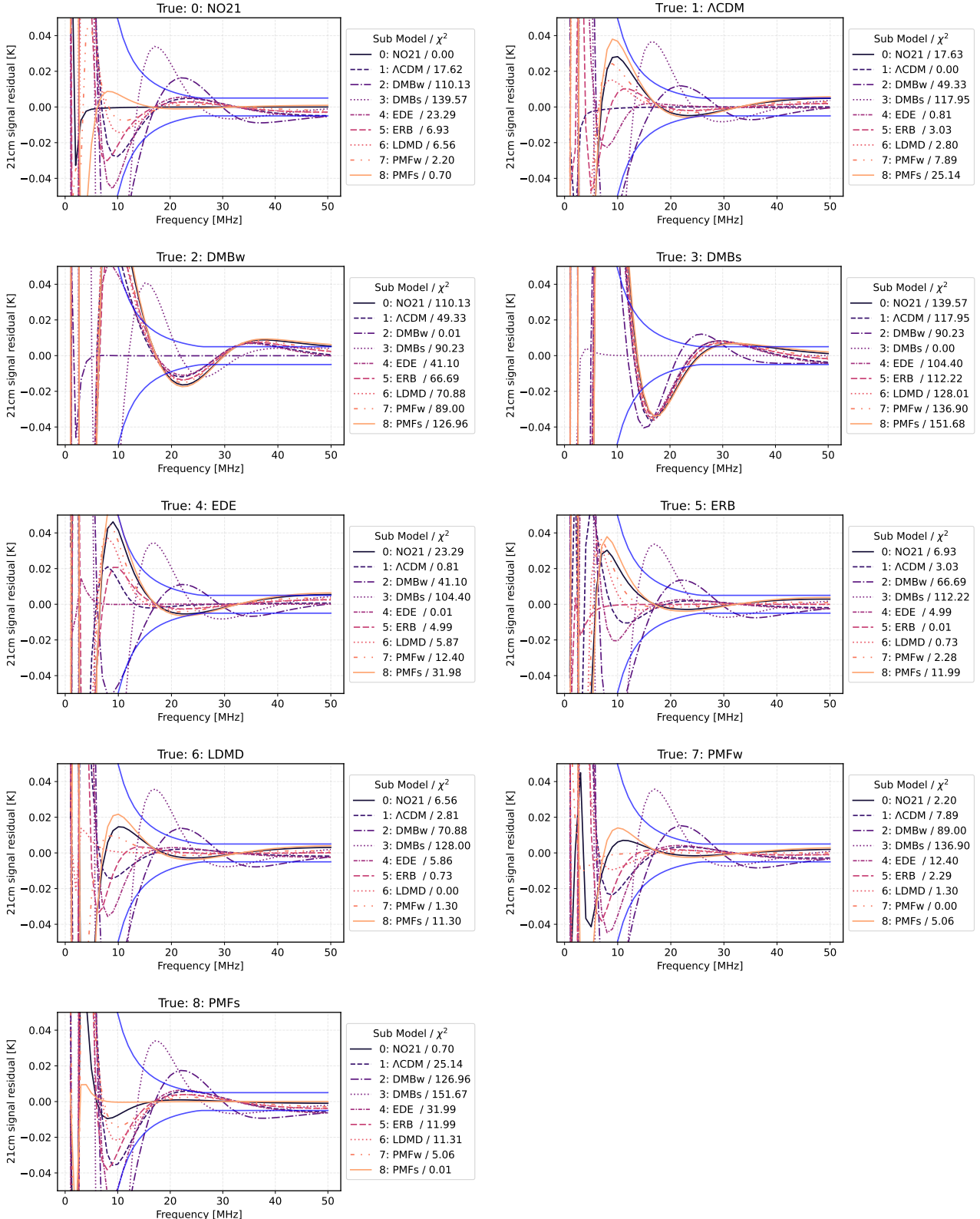


FIG. 6. Residual after signal and foreground subtraction with maximum likelihood sample. The  $\chi^2$  value is also listed in label. Assuming 10000 hours from 1MHz to 50MHz.

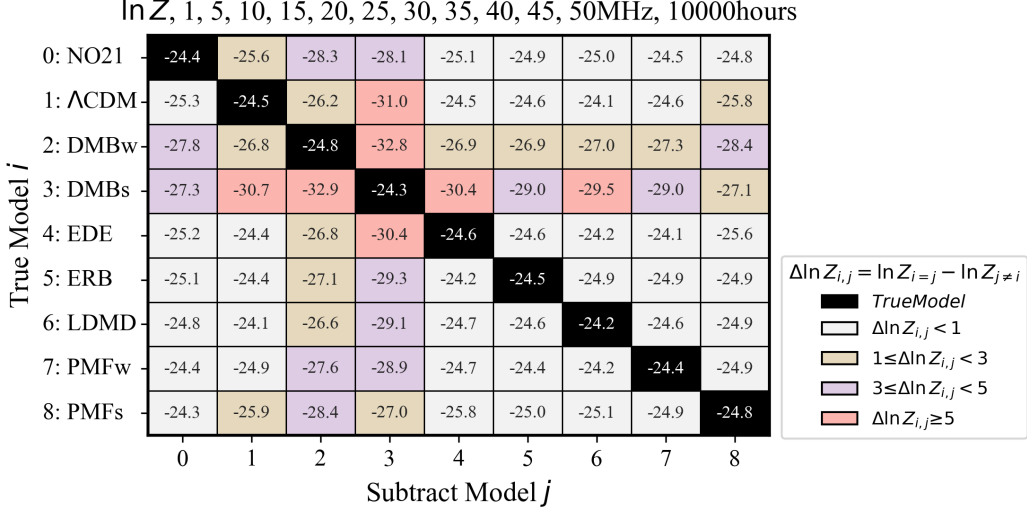


FIG. 7. Same as Figure 5, but assuming observation at 1, 5, 10, 15, 20, 25, 30, 35, 40, 45, 50 MHz.

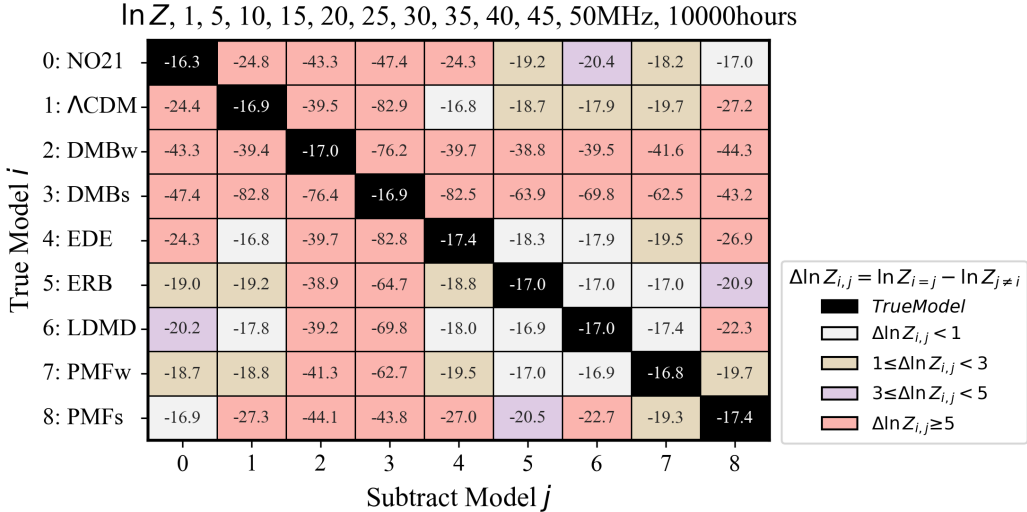


FIG. 8. Same as Figure 7, but assuming reduction of noise level by a factor of  $1/\sqrt{5}$  and minimum noise level is 1mK.

- C. Lonsdale, R. MacDowall, J. Mirocha, J. Muñoz, B. Nhan, J. Pober, D. Rapetti, A. Rogers, and K. Tauscher, Dark Cosmology: Investigating Dark Matter & Exotic Physics in the Dark Ages using the Redshifted 21-cm Global Spectrum, *BAAS* **51**, 6 (2019), arXiv:1902.06147 [astro-ph.CO].
- [14] J. O. Burns, R. Bradley, K. Tauscher, S. Furlanetto, J. Mirocha, R. Monsalve, D. Rapetti, W. Purcell, D. Newell, D. Draper, R. MacDowall, J. Bowman, B. Nhan, E. J. Wollack, A. Fialkov, D. Jones, J. C. Kasper, A. Loeb, A. Datta, J. Pritchard, E. Switzer, and M. Bicay, A Space-based Observational Strategy for Characterizing the First Stars and Galaxies Using the Redshifted 21 cm Global Spectrum, *ApJ* **844**, 33 (2017), arXiv:1704.02651 [astro-ph.IM].
- [15] X. Chen, J. Yan, L. Deng, F. Wu, L. Wu, Y. Xu, and L. Zhou, Discovering the sky at the longest wavelengths with a lunar orbit array, *Philosophical Transactions of the Royal Society of London Series A* **379**, 20190566 (2021), arXiv:2007.15794 [astro-ph.IM].
- [16] M. J. Bentum, M. K. Verma, R. T. Rajan, A. J. Boonstra, C. J. M. Verhoeven, E. K. A. Gill, A. J. van der Veen, H. Falcke, M. K. Wolt, B. Monna, S. Engelen, J. Rotteveel, and L. I. Gurvits, A roadmap towards a space-based radio telescope for ultra-low frequency radio astronomy, *Advances in Space Research* **65**, 856 (2020), arXiv:1909.08951 [astro-ph.IM].
- [17] M. Sathyaranayana Rao, S. Singh, S. K. S., G. B. S., K. Sathish, R. Somashekar, R. Agaram, K. Kavitha, G. Vishwapriya, A. Anand, N. Udaya Shankar, and

- S. Seetha, PRATUSH experiment concept and design overview, *Experimental Astronomy* **56**, 741 (2023), arXiv:2507.05654 [astro-ph.IM].
- [18] H. A. Tanti, A. Datta, A. Kulkarni, A. Nagulpelli, R. Sali, N. Navale, D. Gharpure, S. Ananthakrishnan, and J. Padmanabhan, Seams: A space mission dedicated to ultra-low frequency radio observations, *Proceedings of the XXXVth URSI General Assembly and Scientific Symposium – GASS 2023* (2023).
- [19] <http://ska-jp.org/treed/>.
- [20] T. Hatae, Y. Yamashiro, S. Yoshiura, Y. Kono, M. Ito, K. Fukuda, S. Oi, H. Takamoto, S. Ikari, K. Kura-hara, T. Takahashi, F. Okamatsu, H. Misawa, H. Kita, H. Nakanishi, K. Yamashita, K. Ichiki, and T. Matsuo, In preparation.
- [21] C. D. Brinkerink, M. J. Arts, M. J. Bentum, A. J. Boonstra, B. Cecconi, A. Fialkov, J. Garcia Gutiérrez, S. Ghosh, J. Grenouilleau, L. I. Gurvits, M. Klein-Wolt, L. V. E. Koopmans, J. Lazendic-Galloway, Z. Paragi, D. Prinsloo, R. T. Rajan, E. Rouillé, M. Ruiter, J. A. Tauber, H. K. Vedantham, A. Vecchio, C. J. C. Verte-gaal, J. C. F. Zandboer, and P. Zucca, The Dark Ages Explorer (DEX): a filled-aperture ultra-long wavelength radio interferometer on the lunar far side, arXiv e-prints , arXiv:2504.03418 (2025), arXiv:2504.03418 [astro-ph.IM].
- [22] J. Burns, G. Hallinan, T.-C. Chang, M. Anderson, J. Bowman, R. Bradley, S. Furlanetto, A. Hegedus, J. Kasper, J. Kocz, J. Lazio, J. Lux, R. MacDowall, J. Mirocha, I. Nesnas, J. Pober, R. Polidan, D. Rapetti, A. Romero-Wolf, A. Slosar, A. Stebbins, L. Teitelbaum, and M. White, A Lunar Farside Low Radio Frequency Array for Dark Ages 21-cm Cosmology, arXiv e-prints , arXiv:2103.08623 (2021), arXiv:2103.08623 [astro-ph.IM].
- [23] X. Chen, F. Gao, F. Wu, Y. Zhang, T. Wang, W. Liu, D. Zou, F. Deng, Y. Gong, K. He, J. Li, S. Sun, N. Suo, Y. Wang, P. Wu, J. Xu, Y. Xu, B. Yue, C. Zhang, J. Zhou, M. Zhou, C. Zhu, and J. Zhu, Large-scale array for radio astronomy on the farside (LARAF), *Philosophical Transactions of the Royal Society of London Series A* **382**, 20230094 (2024), arXiv:2403.16409 [astro-ph.IM].
- [24] S. D. Bale, N. Bassett, J. O. Burns, J. Dorigo Jones, K. Goetz, C. Hellum-Bye, S. Hermann, J. Hibbard, M. Maksimovic, R. McLean, R. Monsalve, P. O'Connor, A. Parsons, M. Pulupa, R. Pund, D. Rapetti, K. M. Rotermund, B. Saliwanchik, A. Slosar, D. Sundkvist, and A. Suzuki, LuSEE 'Night': The Lunar Surface Electromagnetics Experiment, arXiv e-prints , arXiv:2301.10345 (2023), arXiv:2301.10345 [astro-ph.IM].
- [25] S. Iguchi, T. Yamada, Y. Yamasaki, T. Onishi, D. Yamauchi, F. Tsuchiya, K. Takahashi, T. Matsumoto, N. Isobe, T. Iwata, N. Usami, Y. Sekimoto, Y. Miyazaki, T. Saiki, O. Mori, and T. Yoshimitsu, Lunar meter-wave telescope (TSUKUYOMI) as one of Japanese lunar plans, in *Space Telescopes and Instrumentation 2024: Optical, Infrared, and Millimeter Wave*, Society of Photo-Optical Instrumentation Engineers (SPIE) Conference Series, Vol. 13092, edited by L. E. Coyle, S. Matsuura, and M. D. Perrin (2024) p. 130922L.
- [26] Y. Yamasaki, T. Matsumoto, S. Iguchi, T. Onishi, T. Yamada, D. Yamauchi, F. Tsuchiya, K. Takahashi, N. Isobe, T. Iwata, N. Usami, Y. Sekimoto, Y. Miyazaki, T. Saiki, O. Mori, and T. Yoshimitsu, A 1-50 MHz short dipole an-tenna for observing the 21 cm global signal on the Moon, in *Space Telescopes and Instrumentation 2024: Optical, Infrared, and Millimeter Wave*, Society of Photo-Optical Instrumentation Engineers (SPIE) Conference Series, Vol. 13092, edited by L. E. Coyle, S. Matsuura, and M. D. Perrin (2024) p. 1309278.
- [27] R. A. Monsalve, A. E. E. Rogers, J. D. Bowman, and T. J. Mozdzen, Calibration of the EDGES High-band Receiver to Observe the Global 21 cm Signature from the Epoch of Reionization, *ApJ* **835**, 49 (2017), arXiv:1602.08065 [astro-ph.IM].
- [28] B. D. Nhan and R. F. Bradley, Safari - a differential approach to probe the cosmological sky-averaged 21-cm signal, in *2024 United States National Committee of URSI National Radio Science Meeting (USNC-URSI NRSM)* (2024) pp. 58–58.
- [29] G. J. A. Harker, Selection between foreground models for global 21-cm experiments., *MNRAS* **449**, L21 (2015), arXiv:1501.05182 [astro-ph.CO].
- [30] G. Bernardi, J. T. L. Zwart, D. Price, L. J. Greenhill, A. Mesinger, J. Dowell, T. Eftekhari, S. W. Ellingson, J. Kocz, and F. Schinzel, Bayesian constraints on the global 21-cm signal from the Cosmic Dawn, *MNRAS* **461**, 2847 (2016), arXiv:1606.06006 [astro-ph.CO].
- [31] G. J. A. Harker, J. Mirocha, J. O. Burns, and J. R. Pritchard, Parametrizations of the 21-cm global signal and parameter estimation from single-dipole experiments, *MNRAS* **455**, 3829 (2016), arXiv:1510.00271 [astro-ph.CO].
- [32] P. H. Sims and J. C. Pober, Testing for calibration systematics in the EDGES low-band data using Bayesian model selection, *MNRAS* **492**, 22 (2020), arXiv:1910.03165 [astro-ph.CO].
- [33] K. H. Scheutwinkel, W. Handley, and E. de Lera Acedo, Bayesian evidence-driven likelihood selection for sky-averaged 21-cm signal extraction, *PASA* **40**, e016 (2023), arXiv:2204.04491 [astro-ph.CO].
- [34] P. H. Sims, J. D. Bowman, S. G. Murray, J. P. Barrett, R. C. Cappallo, C. J. Lonsdale, N. Mahesh, R. A. Monsalve, A. E. E. Rogers, T. Samson, and A. K. Vydula, A general Bayesian model-validation framework based on null-test evidence ratios, with an example application to global 21-cm cosmology, *MNRAS* **541**, 2262 (2025), arXiv:2502.14029 [astro-ph.CO].
- [35] P. H. Sims, J. D. Bowman, S. G. Murray, J. P. Barrett, R. C. Cappallo, C. J. Lonsdale, N. Mahesh, R. A. Monsalve, A. E. E. Rogers, T. Samson, and A. K. Vydula, A Bayesian approach to modelling spectrometer data chromaticity corrected using beam factors — II. Model priors and posterior odds, *MNRAS* **544**, 2340 (2025), arXiv:2506.20042 [astro-ph.IM].
- [36] W. J. Handley, M. P. Hobson, and A. N. Lasenby, poly-chord: nested sampling for cosmology., *MNRAS* **450**, L61 (2015), arXiv:1502.01856 [astro-ph.CO].
- [37] W. J. Handley, M. P. Hobson, and A. N. Lasenby, POLYCHORD: next-generation nested sampling, *MNRAS* **453**, 4384 (2015), arXiv:1506.00171 [astro-ph.IM].
- [38] R. E. Kass and A. E. Raftery, Bayes Factors, *J. Am. Statist. Assoc.* **90**, 773 (1995).
- [39] Okamatsu et al., in prep.
- [40] S. Seager, D. D. Sasselov, and D. Scott, A New Calculation of the Recombination Epoch, *ApJ* **523**, L1 (1999), arXiv:astro-ph/9909275 [astro-ph].

- [41] S. Seager, D. D. Sasselov, and D. Scott, How Exactly Did the Universe Become Neutral?, *ApJS* **128**, 407 (2000), arXiv:astro-ph/9912182 [astro-ph].
- [42] W. Y. Wong, A. Moss, and D. Scott, How well do we understand cosmological recombination?, *MNRAS* **386**, 1023 (2008), arXiv:0711.1357 [astro-ph].
- [43] D. Scott and A. Moss, Matter temperature during cosmological recombination, *MNRAS* **397**, 445 (2009), arXiv:0902.3438 [astro-ph.CO].
- [44] H. Tashiro, K. Kadota, and J. Silk, Effects of dark matter-baryon scattering on redshifted 21 cm signals, *Phys. Rev. D* **90**, 083522 (2014), arXiv:1408.2571 [astro-ph.CO].
- [45] J. C. Hill and E. J. Baxter, Can early dark energy explain EDGES?, *J. Cosmology Astropart. Phys.* **2018**, 037 (2018), arXiv:1803.07555 [astro-ph.CO].
- [46] J. Dowell and G. B. Taylor, The Radio Background below 100 MHz, *ApJ* **858**, L9 (2018), arXiv:1804.08581 [astro-ph.CO].
- [47] M. Valdés, A. Ferrara, M. Mapelli, and E. Ripamonti, Constraining dark matter through 21-cm observations, *MNRAS* **377**, 245 (2007), arXiv:astro-ph/0701301 [astro-ph].
- [48] H. V. Cane, Spectra of the non-thermal radio radiation from the galactic polar regions., *MNRAS* **189**, 465 (1979).
- [49] D. Seitova and J. Pober, The optical depth of foregrounds for the highest redshift 21 cm signals, *MNRAS* **513**, 5125 (2022), arXiv:2205.07941 [astro-ph.CO].
- [50] R. A. Monsalve, C. Altamirano, V. Bidula, R. Bustos, C. H. Bye, H. C. Chiang, M. Díaz, B. Fernández, X. Guo, I. Hendrickson, E. Hornecker, F. Lucero, H. Mani, F. McGee, F. P. Mena, M. Pessôa, G. Prabhakar, O. Restrepo, J. L. Sievers, and N. Thyagarajan, Mapper of the IGM spin temperature: instrument overview, *MNRAS* **530**, 4125 (2024), arXiv:2309.02996 [astro-ph.IM].
- [51] H. K. Vedantham, L. V. E. Koopmans, A. G. de Bruyn, S. J. Wijnholds, B. Ciardi, and M. A. Brentjens, Chromatic effects in the 21 cm global signal from the cosmic dawn, *MNRAS* **437**, 1056 (2014), arXiv:1306.2172 [astro-ph.IM].
- [52] D. Anstey, E. de Lera Acedo, and W. Handley, A general Bayesian framework for foreground modelling and chromaticity correction for global 21 cm experiments, *MNRAS* **506**, 2041 (2021), arXiv:2010.09644 [astro-ph.IM].
- [53] K. Tauscher, D. Rapetti, and J. O. Burns, Global 21 cm Signal Extraction from Foreground and Instrumental Effects. III. Utilizing Drift-scan Time Dependence and Full Stokes Measurements, *ApJ* **897**, 175 (2020), arXiv:2003.05452 [astro-ph.IM].
- [54] D. Anstey, E. de Lera Acedo, and W. Handley, Use of time dependent data in Bayesian global 21-cm foreground and signal modelling, *MNRAS* **520**, 850 (2023), arXiv:2210.04707 [astro-ph.CO].
- [55] Y. Cong, B. Yue, Y. Xu, Q. Huang, S. Zuo, and X. Chen, An Ultralong-wavelength Sky Model with Absorption Effect, *ApJ* **914**, 128 (2021), arXiv:2104.03170 [astro-ph.GA].
- [56] H. Li, F. Deng, M. Zhou, Y. Xu, and X. Chen, Robust Extraction of Global 21 cm Spectrum from Experiments with a Chromatic Beam Based on Physics-motivated Error Modeling, *ApJ* **997**, 4 (2026), arXiv:2507.13102 [astro-ph.IM].